Three-dimensional finite-difference frequency-domain visco-acoustic wave modeling in vertical transversely isotropic media with sparse direct solvers: application to seismic imaging

S. Operto[a], R. Brossier[b], L. Combe[a], L. Métivier[c], A. Ribodetti[a] et J. Virieux[b]
[a]Géoazur, Université Nice Sophia-Antipolis, CNRS, IRD, OCA, 06560 Valbonne, France
[b]ISTerre, Université Joseph Fourier, Grenocle, France
[c]LJK/ISTerre, Université Joseph Fourier, Grenocle, France
operto@geoazur.unice.fr

Seismic imaging by full waveform inversion (FWI) aims to estimate some physical properties of the subsurface from elastic waves recorded near the surface of the earth. Under certain experimental setup and geological environments, the subsurface can be considered to the first order as a visco-acoustic medium in which it might be necessary to account for anisotropic effects. Starting from the elastodynamic equations for vertical transversely isotropic (VTI) media in which we set the shear wavespeed on the symmetry axis to zero, a visco-acoustic wave equation for VTI media is discretized in the frequency-space domain with a finite-difference method. The corresponding numerical problem is the resolution of a system of linear equations, the solution of which is the monochromatic pressure wavefield and the right-hand side term is the seismic source. The coefficients of the so-called impedance matrix, which relates the pressure wavefield to the source, depend on frequency and subsurface properties that we seek to reconstruct by waveform inversion. The finite-difference stencil is specifically designed to solve this system with sparse direct solvers, which allow for the efficient computing of solutions for multiple right-hand sides one the impedance matrix was LU factorized. The anisotropic finite-different stencil does not lead to extra computational cost relative to the isotropic counterpart. The accuracy of the stencil is first illustrated with several numerical simulations. Second, the relevance of this modeling engine to perform nonlinear waveform inversion of a 3D sea-bottom hydrophone dataset collected in the Valhall oil field (north Sea) is discussed.

1 Introduction

Full waveform inversion (FWI) is a data-fitting inverse problem which allows for the estimation of subsurface parameters from the recordings of seismic waves near the surface with a theoretical spatial resolution of half a wavelength (Virieux and Operto (2009) for a recent review). The forward problem is the resolution of the wave equation for each source of the seismic experiment. In the regime of small deformations that characterize seismic wave propagation, the subsurface can be considered as a linear (visco-)elastic medium. However, the subsurface is often approximated by an acoustic medium in marine exploration geophysics, that allows for the computational burden of seismic modeling to be reduced by two to three orders of magnitude. Seismic modeling can be performed in the time-space domain or in the frequency-space domain (Virieux et al., 2009). One drawback of time-marching approaches is that modeling must be started from scratch each time a new source is considered (3D acquisitions can involve several thousands of sources). A second drawback is related to the implementation of attenuation, which requires to introduce memory variables. In contrast, frequency-domain wave modeling is a boundary-value problem, which requires the resolution of a large and sparse system of linear equations per frequency, the solution of which is the monochromatic wavefield and the right-hand side is the source. In virtue of the correspondence principle, implementation of attenuation in the frequency domain is straightforward through the use of complex-valued wavespeeds (Carcione, 2001). Frequency-domain modeling can be efficiently performed for multiple sources by solving the time-harmonic wave equation with sparse direct solvers (this kind of modeling approach is referred to as DSFDM in the following) : a lower-upper (LU) decomposition of the so-called impedance matrix is performed before computing the solutions by substitutions. Although the LU decomposition is expensive in terms of memory, floating-point operations and communications, Operto et al. (2007) and many others since then have shown the feasibility of 3D DSFDM at low frequencies. Recent developments that take advantage of some low-rank properties of the impedance matrix have further improved the efficiency of 3D DSFDM (Wang et al., 2012; Weisbecker et al., 2013). A resolution analysis of FWI shows that the inversion of the seismic data can be limited to a few discrete frequency components for acquisition geometries that record seismic waves over a broad range of incidence angles (as for fixed-spread sea-bottom acquisition geometries) (Sirgue and Pratt, 2004). In this framework, frequency-domain FWI based on DSFDM can be significantly faster at low frequencies relative to frequency-domain FWI based on time-domain modeling (Brossier et al., 2013).

When a finite-difference method is used to discretize the wave equation, the LU factorization requires designing finite-difference stencil with specifications that differ from those used in finite-difference time-domain (FDTD) modeling (Operto et al., 2007) : both the dimension and the numerical bandwidth of the matrix must be minimized. The first requirement direct us toward 2^{nd}-order wave equation through a parsimonious approach such that a reduced number of wavefield components are computed. Moreover, the stencil should provide a sufficient accuracy for a discretization rule of four grid points per wavelength, which is consistent with the theoretical resolution of FWI. This prevents using 2^{nd}-order accurate stencil. On the other hand, minimization of the numerical bandwidth prevents using high-order accurate stencil. The so-called mixed grid approach (Jo et al., 1996) aims to conciliate these apparently contradictory requirements with two recipes : the first one linearly combines several stiffness matrices that are built on different rotated coordinate systems to mitigate numerical anisotropy. The second one spreads the mass term over the nodes involved in the stencil to minimize numerical dispersion. The resulting stencil has the same numerical bandwidth than a 2^{nd}-order accurate stencil and a similar or even better accuracy than a 4^{th}-order accurate stencil.

The 3D visco-acoustic (isotropic) DSFDM stencil is presented in Operto et al. (2007) and Brossier et al. (2010). Here, we extend this stencil to introduce vertical transverse isotropy (VTI) in 3D visco-acoustic modeling, as it is often mandatory to account for anisotropy in FWI of seismic data. Following Wang et al. (2012), we recast the visco-acoustic VTI wave equation as a 4^{th}-order partial differential equation, starting from the velocity-stress elastodynamic wave equation for VTI media and canceling the shear wavespeed on the symmetry axis (Duveneck and Bakker, 2011). We show how this equation can be easily implemented after a slight adaptation of the isotropic 27-point mixed-grid stencil. Numerical simulation in a realistic VTI model from the Valhall oil field illustrates the potential of the method as a modeling engine for visco-acoustic VTI FWI of ocean-bottom seismic data.

2 Governing equation and finite-difference discretization

2.1 Fourth-order acoustic VTI equation

Let's consider the velocity-stress elastodynamic equation for VTI media with explosive sources s applied on the normal stress components.

$$\begin{aligned}
\partial_t v_x &= b\left(\partial_x\sigma_{xx}+\partial_y\sigma_{xy}+\partial_z\sigma_{xz}\right),\\
\partial_t v_y &= b\left(\partial_x\sigma_{xy}+\partial_y\sigma_{yy}+\partial_z\sigma_{yz}\right),\\
\partial_t v_z &= b\left(\partial_x\sigma_{xz}+\partial_y\sigma_{yz}+\partial_z\sigma_{zz}\right),\\
\partial_t\sigma_{xx} &= c_{11}\partial_x v_x + c_{12}\partial_y v_y + c_{13}\partial_z v_z + \tfrac{c_{11}+c_{12}+c_{13}}{D}\,\partial_t s,\\
\partial_t\sigma_{yy} &= c_{12}\partial_x v_x + c_{11}\partial_y v_y + c_{13}\partial_z v_z + \tfrac{c_{11}+c_{12}+c_{13}}{D}\,\partial_t s,\\
\partial_t\sigma_{zz} &= c_{13}\partial_x v_x + c_{13}\partial_y v_y + c_{33}\partial_z v_z + \tfrac{c_{33}+2c_{13}}{D}\,\partial_t s,\\
\partial_t\sigma_{yz} &= c_{55}\left(\partial_y v_z+\partial_z v_y\right),\\
\partial_t\sigma_{xz} &= c_{55}\left(\partial_x v_z+\partial_z v_x\right),\\
\partial_t\sigma_{xy} &= c_{66}\left(\partial_x v_y+\partial_y v_x\right),
\end{aligned} \tag{1}$$

where v_i denotes the particle-velocity wavefields, σ_{ij} the stress wavefields, c_{ij} the coefficients of the stiffness tensor and b is the buoyancy, the inverse of the density ρ and $D = 2\,c_{11} + 2\,c_{12} + 4\,c_{13} + c_{33}$. The factors of the source term s are chosen to minimize the emission of shear waves at the source position.

We set the shear wave velocity on the symmetry axis to 0 ($c_{55} = c_{66} = 0$) to derive the VTI equation in the acoustic approximation (Duveneck and Bakker, 2011). This leads to :

$$\begin{aligned}
\partial_t v_x &= b\partial_x\sigma_{xx},\\
\partial_t v_y &= b\partial_y\sigma_{yy},\\
\partial_t v_z &= b\partial_z\sigma_{zz},\\
\partial_t g &= c_{11}\left(\partial_x v_x+\partial_y v_y\right) + c_{13}\partial_z v_z + s_g\partial_t s,\\
\partial_t q &= c_{13}\left(\partial_x v_x+\partial_y v_y\right) + c_{33}\partial_z v_z + s_q\partial_t s,
\end{aligned} \tag{2}$$

where $g = \sigma_{xx} = \sigma_{yy}$, $q = \sigma_{zz}$, $s_g = \frac{2\,c_{11}+c_{13}}{D}$, $s_q = \frac{c_{33}+2\,c_{13}}{D}$ and $D = 4\,c_{11} + 4\,c_{13} + c_{33}$. In the acoustic approximation of VTI seismic modeling, we shall approximate the pressure p as $p = \frac{1}{3}(2g + q)$. To derive equation 2, we have used the relationship $c_{12} = c_{11} - 2c_{66}$ in VTI media, which reduces to $c_{12} = c_{11}$ when $c_{66} = 0$. In isotropic media, $s_g = s_q = 1$.

Applying a Fourier transform with respect to time and eliminating the particle-velocity wavefield from the system gives a system of 2^{nd}-order partial differential equations for the stress fields q and q :

$$\frac{\omega^2}{\kappa_0}\,g \;+\; (1+2\epsilon)\,(\mathcal{X}+\mathcal{Y})\,g + \sqrt{1+2\delta}\,\mathcal{Z}\,q = \frac{\omega^2\,s_g}{\kappa_0}\,s \tag{3}$$

$$\frac{\omega^2}{\kappa_0}\,q \;+\; \sqrt{1+2\delta}\,(\mathcal{X}+\mathcal{Y})\,g + \mathcal{Z}\,q = \frac{\omega^2\,s_q}{\kappa_0}\,s. \tag{4}$$

In Eqs. -4, we introduce a subsurface parameterization defined by the vertical wavespeed V_{P0} and the dimensionless Thomsen's parameters δ and ϵ. The bulk modulus on the symmetry axis is denoted by $\kappa_0 = \rho\,V_{P0}^2$. The c_{ij} coefficients are related to these parameters by :

$$\begin{aligned}
c_{33} &= \rho\,V_{P0}^2,\\
c_{11} &= \rho\,V_{P0}^2\sqrt{1+2\epsilon},\\
c_{13} &= c_{33}\,\sqrt{1+\delta} = \rho\,V_{P0}^2\,\sqrt{1+\delta}.
\end{aligned}$$

For sake of compactness, the following notations for the 2^{nd}-order differential operators are introduced :

$$\mathcal{X} = \frac{1}{\xi_x}\partial_x\frac{b}{\xi_x}\partial_x,\quad \mathcal{Y} = \frac{1}{\xi_y}\partial_y\frac{b}{\xi_y}\partial_y,\quad \mathcal{Z} = \frac{1}{\xi_z}\partial_z\frac{b}{\xi_z}\partial_z.$$

We implement perfectly-matched layer (PML) absorbing conditions through the 1D functions $\xi_x = 1 + i\frac{\gamma_x}{\omega}$, $\xi_y = 1 + i\frac{\gamma_y}{\omega}$ and $\xi_z = 1 + i\frac{\gamma_z}{\omega}$, where functions γ_x, γ_y and γ_z control the damping of the wavefield in the PMLs (Operto et al., 2007). The source excitation in the frequency domain is denoted by s and we found $s_g = \frac{2(1+2\,\epsilon)+\sqrt{1+2\,\delta}}{D}$ and $s_q = \frac{1+2\,\sqrt{1+2\,\delta}}{D}$ with $D = 4\,\sqrt{1+2\,\epsilon} + 4\,\sqrt{1+2\,\delta} + 1$ for explosive source.

We aim to eliminate q from equations 2.1-4 to derive a 4^{th}-order equation for g. We found

$$q = \frac{1}{\sqrt{1+2\delta}}\,g + \frac{2(\epsilon-\delta)\kappa_0}{\omega^2\,\sqrt{1+2\delta}}\,(\mathcal{X}+\mathcal{Y})\,g + \left(s_q - \frac{1}{\sqrt{1+2\delta}}\,s_g\right)s. \tag{5}$$

Injecting the expression of q in equation 2.1 gives the 4^{th}-order equation satisfied by g :

$$\omega^2\left[\frac{\omega^2}{\kappa_0} + (1+2\epsilon)\,(\mathcal{X}+\mathcal{Y}) + \sqrt{1+2\delta}\mathcal{Z}\frac{1}{\sqrt{1+2\delta}}\right]g \tag{6}$$

$$+2\,\sqrt{1+2\delta}\mathcal{Z}\frac{\kappa_0(\epsilon-\delta)}{\sqrt{1+2\delta}}\,(\mathcal{X}+\mathcal{Y})\,g$$

$$= \frac{\omega^4\,s_g}{\kappa_0}\,s - \omega^2\,\sqrt{1+2\delta}\,\mathcal{Z}\left(s_q - \frac{1}{\sqrt{1+2\delta}}\,s_g\right)s. \tag{7}$$

For homogeneous δ, equation 7 shows that the VTI equation can be decomposed into an elliptic anisotropic operator ($\frac{\omega^2}{\kappa_0} + (1+2\epsilon)\,(\mathcal{X}+\mathcal{Y}) + \mathcal{Z}$) and an anellipticity term ($2\,\mathcal{Z}\kappa_0(\epsilon-\delta)\,(\mathcal{X}+\mathcal{Y})$).

2.2 Finite-difference discretization

The VTI acoustic equation, eq. 7, is implemented after a slight adaptation of the isotropic stencil (Operto et al., 2007). The isotropic and VTI wave equations can be written in compact form as :

$$Isotropic : [\mathbf{M}+\mathbf{S}]\,\mathbf{p} = \mathbf{s}; \tag{8}$$

$$VTI : \omega^2\,\{[\mathbf{M}_e+\mathbf{S}_e]\,\mathbf{g}\} + \mathbf{E}\,\mathbf{g} = \mathbf{A}\,\mathbf{g} = \mathbf{s}',\ \mathbf{q} = \mathbf{B}\,\mathbf{g} + \mathbf{s}",$$
$$\text{with}\quad \mathbf{p} = (1/3)(2\,\mathbf{g}+\mathbf{q}). \tag{9}$$

The mass matrix $\mathbf{M}_e$ is built with the same anti-lumped mass strategy than the isotropic counterpart $\mathbf{M}$.

The elliptic stiffness matrix $\mathbf{S}_e$ is easily inferred from the isotropic counterpart $\mathbf{S}$. First, we multiply each coefficient of $\mathbf{S}$ that involves an horizontal spatial derivative with $(1+2\epsilon_k)$ where k is the index of the row to which the coefficient belongs. Second, we need to form the matrix-vector product $\sqrt{1+2\delta}\mathcal{Z}(g/\sqrt{1+2\delta})$. We first discretize $\sqrt{1+2\delta}\mathcal{Z}$ by multiplying each coefficient of $\mathbf{S}$ that involves a vertical spatial derivative with $\sqrt{1+2\delta_k}$, where k is the index of the row to which the coefficient belongs. Then, we inject the discrete expressions of $g/\sqrt{1+2\delta}$ in the matrix-vector product, that amounts to divide each coefficient that involves a vertical spatial derivative in $\mathbf{S}$ by $\sqrt{1+2\delta_l}$, where l is the column index to which the coefficient belongs.

The anelliptic matrix $\mathbf{E}$ is discretized with a parsimonious 2^{nd}-order accurate staggered-grid stencil, which preserves the spatial support of the stencil over two grid intervals. Once $\mathbf{g}$ is computed, we infer $\mathbf{q}$ from eq. 5. We discretize the matrix $\mathbf{B}$ with a 2^{nd}-order accurate stencil, although any other stencil can be used as computation of q does not require system resolution.

VTI modeling is performed at the same cost than isotropic modeling. A dispersion analysis in homogeneous

media shows that the weighting coefficients of the mixed-grid stencil that were obtained for the isotropic equation can be re-used for modeling in elliptic media with the same discretization rule of 4 grid points per wavelength. These coefficients were found quite insensitive to the value of ϵ.

2.3 Numerical examples

We validate the DSFDM method against a $O(\Delta t^2, \Delta x^4)$ staggered-grid finite-difference time-domain (FDTD) method. During FDTD modeling, monochromatic wavefields are extracted on the fly in the loop over time steps by discrete Fourier transform (Sirgue et al., 2007). During DSFDM, we use the sparse direct solver MUMPS (Amestoy et al., 2000) to perform the LU factorization, which was computed in single and double precision without differences in the results. The fill-reducing matrix ordering is performed with a nested-dissection algorithm. We observed some instabilities in the PMLs for VTI media, when the grid interval is significantly smaller that a quarter of a wavelength. Pragmatically, we force the medium to be elliptic in the PMLs to avoid these instabilities.

2.4 Layer model

We consider a subsurface model composed of two homogeneous layers delineated by a flat reflector to assess the accuracy of the mixed-grid stencil when the wavefield interacts with a sharp discontinuity. We use the same numerical grid to perform the DSFDM and the FDTD simulations such that the reflector discretization is identical for each numerical method. The vertical wavespeed is 2 km/s and 2.5 km/s in the upper and lower layers, respectively, while the density is 1000 kg/m^3 and 1500 kg/m^3, respectively. The upper layer is elliptic with $\delta = \epsilon = 0.05$, while $\delta = 0.1$ and $\epsilon = 0.2$ in the bottom layer. The modeled frequency is 10 Hz. The subsurface model have dimensions (5km,5km,2km) and is discretized with a grid interval of 25m leading to a 201x201x81 finite-difference grid. A 10-Hz frequency leads to a discretization rule of eight grid points per minimum wavelength. The length of the time-domain simulation is 12 s.

Monochromatic wavefields computed with DSFDM and FDTD match well from a qualitative viewpoint (Fig. 1). Direct comparison between DSFDM and FDTD solutions shows an excellent match when the propagation direction follows one of the three Cartesian directions (Fig. 1(a-c)), while phase and amplitude mismatches are visible when the propagation direction does not follow a Cartesian direction (Fig. 1(d-f)). We interpret these mismatches as the numerical anisotropy of the FDTD stencil.

2.5 Valhall model

We present simulations in a VTI visco-acoustic model of the Valhall oil field (Fig. 2(a-b)) that was developed by reflection traveltime tomography (courtesy of BP). The water depth is around 70m. The subsurface is characterized by soft sediments above low-velocity gas layers. The reservoir at 2.5 km in depth delineates a sharp positive velocity contrast. The maximum anisotropy reaches a value of 15 percent. The footprint of anisotropy on FWI is discussed in Prieux et al. (2011). The model dimensions are 16km x 9km x 4.5km.

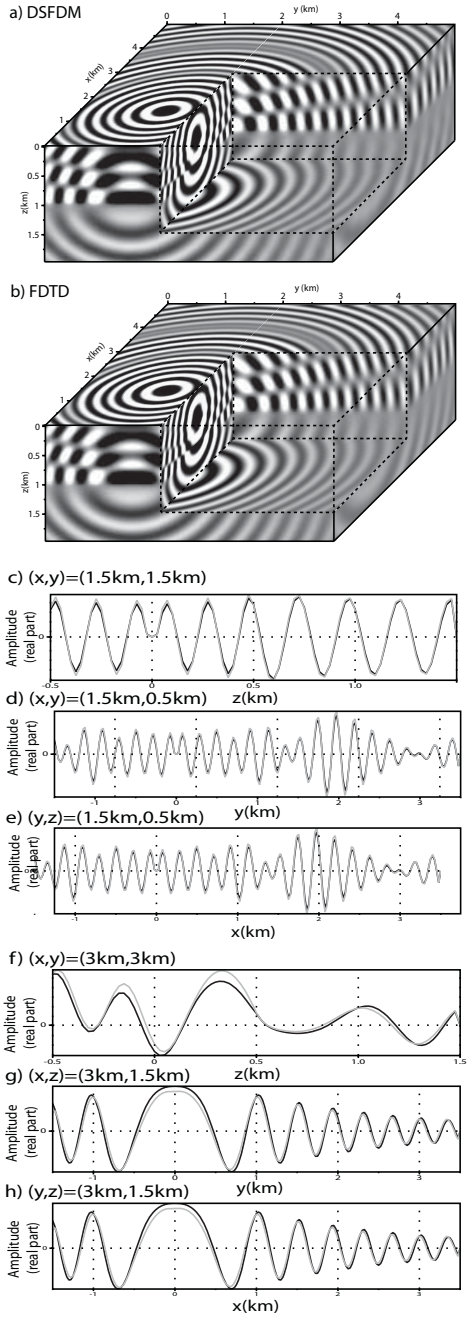

Figure 1 – Layer model. (a) DSFDM monochromatic wavefield. Frequency is 10 hz. (b) FDTD monochromatic wavefield. (c-e) Direct comparison between DSFDM and FDTD solutions along x-, y-, z- profiles running across the source position. Amplitudes are roughly corrected for geometrical spreading. (f-h) Same as (c-e) for profiles extracted across the position (x,y,z)=(3km,3km,1.5km).

We compare VTI monochromatic wavefields computed with DSFDM and FDTD for the 7-Hz frequency and a source located on the sea bottom at (x=3.1km,y=13km,z=0.07km). The grid intervals are 50m and 25 m for DSFDM and FDTD, respectively. This gives a discretization of 4 grid points per minimum wavelength in DSFDM. The grid dimensions are 182 x 322 x 92 for DSFDM. Adding eight grid points in the PMLs leads to 6.7 millions of unknowns. A free surface condition is set on top of the model. The source is positioned in the finite-difference grid with a sinc parameterization (Hicks, 2002). The length of the FDTD

simulation is 20s and guarantees that the steady-state regime is reached. The DSFDM simulations were performed on 16 Intel(R) Xeon(R) CPU X5660 @ 2.80GHz bi-processor nodes. Each node is equipped with 12 cores and 48Gb of shared memory. The connecting network is Infiniband and the compiler is INTEL. We distributed the LU factorization and the substitution step over 16 Message-Passing-Interface (MPI) processes (1 per node) and we used 12 threads per MPI process for basic linear algebra tasks performed with a threaded distribution of the Basic Linear Algebra Subroutines (BLAS3). The LU factorization took 12.5mn and the substitution step took 0.75s per source. The total amount of memory used during the LU factorization for 515Gb. The agreement between DSFDM and FDTD wavefields can be qualitatively assessed in Fig. 2(c-d)). Comparison between real data and DSFDM solutions extracted at 5m in depth below the sea surface shows a good agreement owing to the fact that the smooth Valhall model does not predict the full wavefield complexity (Fig. 3). In particular, we notice some mismatches at offsets where reflected waves and low-velocity layers have a significant footprint in the monochromatic wavefield. However the VTI DSFDM solutions clearly better matches the recorded data than the isotropic counterpart, hence supporting our anisotropic implementation of frequency-domain modeling

3 Seismic imaging by FWI

Our finite-difference frequency-domain method can be used as a modeling engine to estimate several subsurface parameters m at each node of the computational domain by nonlinear frequency-domain FWI. Optimization parameters can be a subset of parameters $(V_{P0}, \rho, \delta, \epsilon)$ or of any other combination of them (see Operto et al. (2013) for a discussion on the role of the parameterization on multiparameter FWI). FWI aims to minimize the misfit between seismic data d collected near the surface and modeled data. The data misfit is generally the difference between the recorded and modeled data and the least-squares norm C of this difference provides a possible measure of the distance between recorded and modeled data.

The optimization problem can be stated as

$$\min_m C(m) = \min_m \frac{1}{2} \sum_\omega \sum_s \sum_r \|(R_r p(m))_{\omega,s} - d_{\omega,s,r}\|_2^2. \quad (10)$$

where s and r denote the sources and receivers, respectively, p is the modeled pressure wavefield, and R_r is a sampling operator with extract the values of p at the position of r.

Minimization of C around a starting model m_0 gives the model perturbation δm

$$\delta m = -H^{-1} \nabla C, \quad (11)$$

where ∇C is the gradient of the misfit function and H is the Hessian, the second derivative of C. The updated model is given by $m_1 = m_0 + \delta m$ and this updating can be iterated in a nonlinear way using the final model of iteration k as the initial model of the next iteration.

The gradient of the misfit function is computed with the adjoint-state method, which requires the solving of two forward problems per source (Plessix, 2006). The action of the Hessian on the gradient can be accounted for without

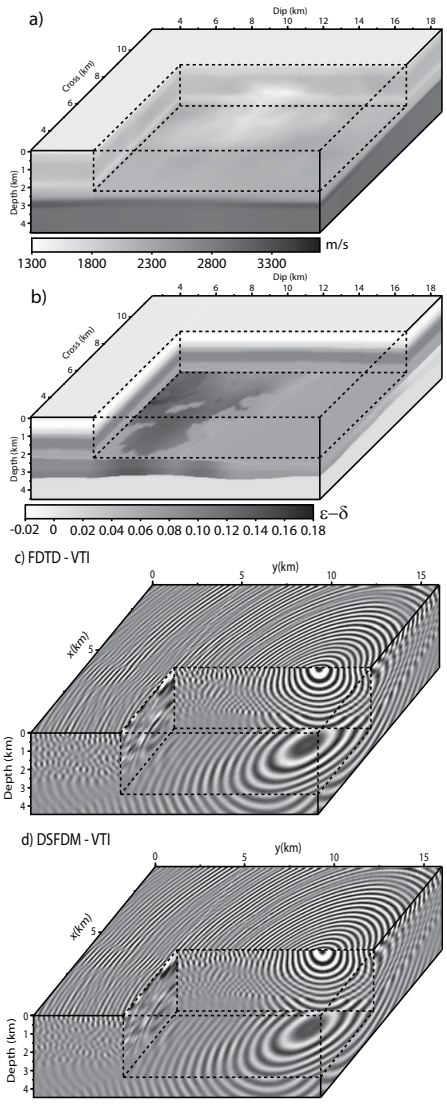

FIGURE 2 – (a-b) Valhall model. (a) V_{P0}. (b) $\epsilon - \delta$. (c-d) Seven-Hz wavefield. (c) FDTD. (d) DSFDM.

explicitly building the Hessian using matrix-free methods such as the quasi-Newton l-BFGS method (Nocedal and Wright, 2006) or the truncated Newton method (Métivier et al., 2013).

To compute ∇C with the adjoint-state method, we augment the misfit function with constraints corresponding to the forward-problem (state) equations

$$\begin{aligned}
\mathcal{L}(g,q,p,a_1,a_2,a_3,m) &= \sum_\omega \sum_s \sum_r \|R_r p_{\omega,s} - d_{\omega,s,r}\|^2 \\
&+ \Re < a_{1_{\omega,s}}, A(\omega,m) g_{\omega,s} - b_{\omega,s} >_\Omega \\
&+ \Re \sum_\omega \sum_s < a_{2_{\omega,s}}, q_{\omega,s} - B(\omega,m) g_{\omega,s} - s'_{\omega,s} >_\Omega \\
&+ \Re \sum_\omega \sum_s < a_{3_{\omega,s}}, p_{\omega,s} - \frac{1}{3}(2g_{\omega,s} + q_{\omega,s}) >_\Omega, \quad (12)
\end{aligned}$$

where Ω is the domain spanned by the computational grid and $a_{1_{\omega,s}}, a_{2_{\omega,s}}, a_{3_{\omega,s}}$ are the adjoint-state variables associated with each source and frequency. The real part $\Re$ is introduced in front of the inner products because the state and variables are complex-valued while the misfit function is real valued. For any realizations of the state equations, $\nabla_m C = \nabla_m L$. The adjoint-state variables are chosen at the saddle points of the Lagrangian $\mathcal{L}$ with

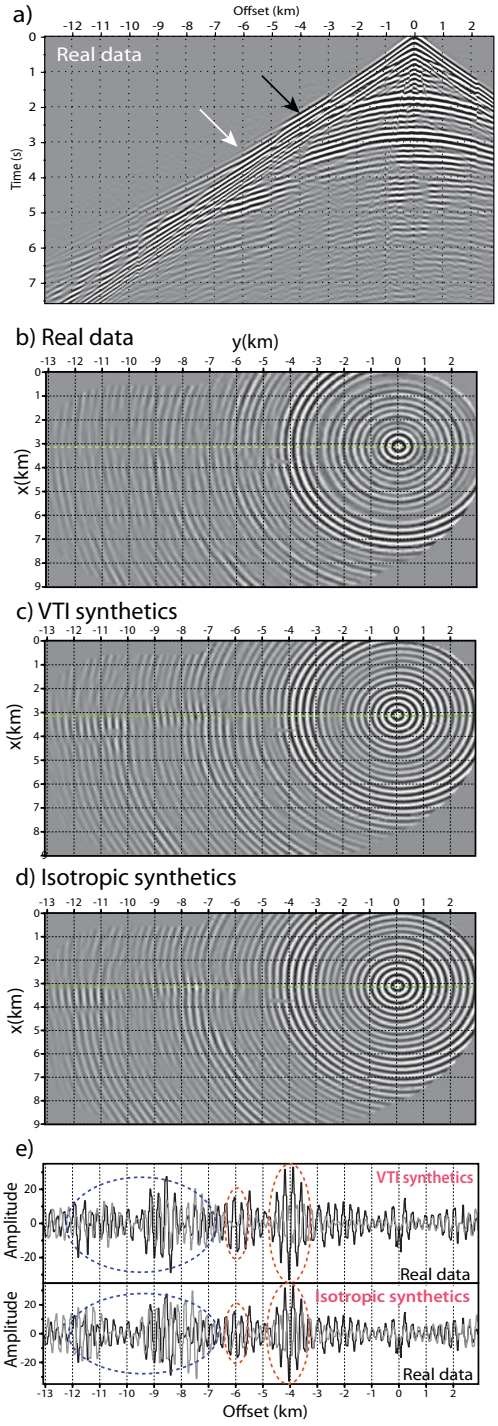

FIGURE 3 – Valhall. (a) Real receiver gather. Black and white arrows point a subcritical reflection and a polarity reversal in the first arrival, respectively. (b-c) Real data (b) and DSFDM data (c) for the 7-Hz frequency. DSFDM data were multiplied with the source signature that was estimated by matching the real data with the DSFDM Green functions. (d) Comparison along the yellow line in (b-c) between real data (black) and VTI/isotropic (top/bottom) DSFDM data (gray), plotted with an amplitude gain with offset. Mismatches (red ellipses) are shown at offsets where the Valhall model does not predict the wavefield complexity (arrows in (a)). VTI synthetics match better the real data than isotropic ones at long offsets where anisotropic effects are significant (blue ellipse).

respect to the state variables g, q and p. After noting that $a_{3_{\omega,s}} = \sum_r R^t \left(R_r p_{\omega,s} - d_{\omega,s,r}\right)^*$, the adjoint-state equations satisfied by a_1 and a_2 are given by

$$A^t\, a^*_{1_{\omega,s}} = \left(\frac{1}{3}B^t(\omega,m) + \frac{2}{3}I\right)\sum_r R^t \left(R_r p_{\omega,s} - d_{\omega,s,r}\right)^* .$$
$$a_{2_{\omega,s}} = \frac{1}{3}\sum_r R^t \left(R_r p_{\omega,s} - d_{\omega,s,r}\right)^* . \qquad (13)$$

The gradient of C is given by

$$\nabla C_m = \sum_\omega \sum_s \Re\left(< a_{1_{\omega,s}}, \frac{\partial A(\omega,m)}{\partial m} g_{\omega,s} >_\Omega \right.$$
$$\left. + < a_{2_{\omega,s}}, \frac{\partial B(\omega,m)}{\partial m} g_{\omega,s} >_\Omega \right). \qquad (14)$$

We can neglect the second term if we assume that the subsurface is known at the receiver positions. Gradient computation requires to perform one LU factorization of $\mathbf{A}$ per frequency and two substitution steps per source s to compute the incident wavefield g and the adjoint wavefield a_1. The direct solver MUMPS provides the necessary facilities to apply either A or its transpose to a vector for the computation of these two wavefields. The performances of isotropic frequency-domain FWI based on FDTD and DSFDM are compared in Brossier et al. (2013) for the Valhall survey, which involves 2302 hydrophone receivers and 50,000 shots (during FWI, receivers are processed as sources to reduce the number of modeling taking advantage of the spatial reciprocity of the Green functions). When frequency-domain FWI is performed with FDTD, monochromatic wavefields are extracted on the fly in the loop over time steps by discrete Fourier transform or phase sensitivity detection (Nihei and Li, 2007; Sirgue et al., 2007), allowing for the extraction of several frequency components without significant computational burden. Time-domain modeling was performed on an IBM Blue Gene P, equipped with single-processor Power PC 450 nodes, interconnected through the IBM 3D toroidal network. Two-level parallelism is implemented by distributing 512 sources over the computing processors and by decomposing the subsurface model in four sub-domains. Two groups of 5 and 9 frequencies are successively inverted in the frequency bands [3.5-4] Hz and [4-5] Hz, respectively. FWI based on DSFDM was performed on a cluster equipped with Intel Westmere bi-processor nodes, connected to a high-speed Mellanox QDR 40 Gb/s Infiniband network. Each node is composed of 12 computing cores at 2.26 GHz, which share 72 Gb of core memory. Two discrete frequencies, 3.8 Hz and 4.5 hz, are successively inverted using 6 nodes. For these architectures and experimental setup, FWI based on DSFDM was 18-times faster than FWI based on FDTD. The two inversions used the same amount of memory (around 500 Gb) although the memory usage is quite different in the two cases : in DSFDM, the memory is mainly used to store the LU factors and only a limited number of sources are processed in parallel during the substitution step taking advantage of BLAS3 library before moving to another set of sources. In contrast, a number of sources as large as possible is processed in parallel during FDTD modeling (as almost no communication is required by the source distribution), which requires the distributed storage in core of the corresponding wavefield solutions.

We should add that the performances of DSFSDM can be further improved by using a block low-rank version of the MUMPS solver (Weisbecker et al., 2013). These conclusions apply to the anisotropic scheme presented in this study since it does not introduce computational burden relative to the isotropic case.

4 Conclusion

We have presented a parsimonious finite-difference frequency-domain method that is suitable to perform visco-acoustic modeling in vertical transversely isotropic media with sparse direct solver. This modeling engine is designed for FWI of fixed-spread data in which anisotropic and attenuation effects can be introduced without extra cost relative to isotropic imaging. A discretization rule of four grid points per wavelength is enough to guarantee accurate simulations and is consistent with the theoretical resolution of FWI. The implementation of the block low-rank approximation in sparse direct solver should still increase the computational efficiency of the method.

Acknowledgments

This study was funded by the SEISCOPE II consortium (*http ://seiscope2.osug.fr*). This study was granted access to the HPC facilities of SIGAM (Observatoire de la Cote d'Azur).

Références

Amestoy, P., Duff, I. S., and L'Excellent, J. Y. (2000). Multifrontal parallel distributed symmetric and unsymmetric solvers. *Computer Methods in Applied Mechanics and Engineering*, 184(2-4) :501–520.

Brossier, R., Etienne, V., Hu, G., Operto, S., and Virieux, J. (2013). Performances of 3D frequency-domain full-waveform inversion based on frequency-domain direct-solver and time-domain modeling : application to 3D OBC data from the Valhall field. *International Petroleum Technology Conference, Beijing, China*, page IPTC 16881.

Brossier, R., Etienne, V., Operto, S., and Virieux, J. (2010). Frequency-domain numerical modelling of visco-acoustic waves based on finite-difference and finite-element discontinuous galerkin methods. In Dissanayake, D. W., editor, *Acoustic Waves*, pages 125–158. SCIYO.

Carcione, J. M. (2001). *Wave fields in real media, Theory and numerical simulation of wave propagation in anisotropic, an elastic and porous media*. Pergamon Press.

Duveneck, E. and Bakker, P. M. (2011). Stable P-wave modeling for reverse-time migration in tilted TI media. *Geophysics*, 76(2) :S65–S75.

Hicks, G. J. (2002). Arbitrary source and receiver positioning in finite-difference schemes using kaiser windowed sinc functions. *Geophysics*, 67 :156–166.

Jo, C. H., Shin, C., and Suh, J. H. (1996). An optimal 9-point, finite-difference, frequency-space 2D scalar extrapolator. *Geophysics*, 61 :529–537.

Métivier, L., Bretaudeau, F., Brossier, R., Operto, S., and Virieux, J. (2013). Full waveform inversion and the truncated newton method : quantitative imaging of complex subsurface structures. *Geophysical Prospecting*, In press.

Nihei, K. T. and Li, X. (2007). Frequency response modelling of seismic waves using finite difference time domain with phase sensitive detection (TD-PSD). *Geophysical Journal International*, 169 :1069–1078.

Nocedal, J. and Wright, S. J. (2006). *Numerical Optimization*. Springer, 2nd edition.

Operto, S., Brossier, R., Gholami, Y., Métivier, L., Prieux, V., Ribodetti, A., and Virieux, J. (2013). A guided tour of multiparameter full waveform inversion for multicomponent data : from theory to practice. *The Leading Edge*, September, Special section Full Waveform Inversion :1040–1054.

Operto, S., Virieux, J., Amestoy, P., L'Éxcellent, J.-Y., Giraud, L., and Ben Hadj Ali, H. (2007). 3D finite-difference frequency-domain modeling of visco-acoustic wave propagation using a massively parallel direct solver : A feasibility study. *Geophysics*, 72(5) :SM195–SM211.

Plessix, R. E. (2006). A review of the adjoint-state method for computing the gradient of a functional with geophysical applications. *Geophysical Journal International*, 167(2) :495–503.

Prieux, V., Brossier, R., Gholami, Y., Operto, S., Virieux, J., Barkved, O., and Kommedal, J. (2011). On the footprint of anisotropy on isotropic full waveform inversion : the Valhall case study. *Geophysical Journal International*, 187 :1495–1515.

Sirgue, L., Etgen, T. J., Albertin, U., and Brandsberg-Dahl, S. (2007). System and method for 3D frequency-domain waveform inversion based on 3D time-domain forward modeling. *US Patent Application Publication*, US2007/0282535 A1.

Sirgue, L. and Pratt, R. G. (2004). Efficient waveform inversion and imaging : a strategy for selecting temporal frequencies. *Geophysics*, 69(1) :231–248.

Virieux, J. and Operto, S. (2009). An overview of full waveform inversion in exploration geophysics. *Geophysics*, 74(6) :WCC1–WCC26.

Virieux, J., Operto, S., Ben Hadj Ali, H., Brossier, R., Etienne, V., Sourbier, F., Giraud, L., and Haidar, A. (2009). Seismic wave modeling for seismic imaging. *The Leading Edge*, 28(5) :538–544.

Wang, S., Xia, J., de Hoop, M. V., and Li, X. S. (2012). Massively parallel structured direct solver for equations describing time-harmonic qP-polarized waves in TTI media. *Geophysics*, 77(3) :T69 – T82.

Weisbecker, C., Amestoy, P., Boiteau, O., Brossier, R., Buttari, A., L'Excellent, J.-Y., Operto, S., and Virieux, J. (2013). 3D frequency-domain seismic modeling with a block low-rank algebraic multifrontal direct solver. In *SEG Technical Program Expanded Abstracts 2007*.